Front. Earth Sci. 2024, 18(1): 112−126
https://doi.org/10.1007/s11707-022-1047-5

RESEARCH ARTICLE

Global precipitation change during the Holocene: a combination of records and simulations

Wangting YE, Yu LI (✉)

Key Laboratory of Western China's Environmental Systems (Ministry of Education), College of Earth and Environmental Sciences, Center for Hydrologic Cycle and Water Resources in Arid Region, Lanzhou University, Lanzhou 730000, China

Abstract Precipitation can shape our climate both in the present and the future. Even though we have made significant advances in studying the mechanisms of millennial-scale climate changes through high-resolution records, we still cannot quantitatively characterize the global spatiotemporal precipitation variations within the Holocene. Therefore, we developed a new approach to integrating data from 349 globally distributed records and climate models to reconstruct regional and global precipitation patterns over the last 12000 years. Our results reveal that precipitation reconstructions can be divided into monsoon-driven and westerly driven patterns. The results suggest that an arid climate was experienced in the late glacial and early Holocene epoch (~12−7.4 cal ka BP), attaining a middle Holocene optimum (~7.4−3.5 cal ka BP), and drier after the middle Holocene. According to our reconstructions, the global precipitation reconstruction increased from the early Holocene until 3.8 cal ka BP and then subsequently decreased. In addition, our reconstructions better reproduce the low-frequency events and extreme precipitation at the millennial scale in the hemispheres, but the performance of the reconstructions in the equatorial Pacific and the Southern Hemisphere of Africa and the Americas is controversial. The resolution of the record and the simulation capability of the climate model remain important means to improve our understanding of past climate change.

1 Introduction

The hydrologic cycle is the continuous exchange of water between the Earth's surface and its atmosphere, which plays an essential role in the survival of life forms. Precipitation, one of the key processes of this cycle, can shape the past and present ecological environment (Yang et al., 2014; Tierney et al., 2015; Vörösmarty et al., 2000; Zwart et al., 2017). Even if global climate simulations predict widespread wetter conditions in the future, precipitation patterns, such as the decline in precipitation and longer than usual periods of rain, have become more common worldwide in recent decades as the global climate continues to warm (Yang et al., 2014; Schewe and Levermann, 2017). Therefore, quantitative studies of past precipitation are essential for understanding future climate and developing resistance and adaptive responses to global warming challenges.

Due to the rapid development of instrumentation in recent decades, paleoclimate studies based on climate proxies have developed rapidly. The information gained from marine and lacustrine deposits, cave sediments, lake-level data, and pollen records has been used for reconstructions of past precipitation during the Holocene (Li et al., 2009, 2014, 2018; Abram et al., 2016; Gagen et al., 2016; Li and Xu, 2016). Numerous studies have confirmed that local summer insolation dominates the precipitation change in the millennial-scale monsoon region at low latitudes. $\delta^{18}O$ (‰) evidence from Dongge Cave and high-resolution bulk titanium content from the Gulf of Cariaco reflect the local precipitation pattern is in line with the local summer insolation (Werne et al., 2000; Dykoski et al., 2005; Duan et al., 2014), and the evidence also shows the rapid shifts in vegetation in the Sahel-Sahara region of Africa monsoons (deMenocal et al., 2000). In addition to insolation, the ocean and atmospheric circulation are other factors driving precipitation patterns on millennial to centennial scales. In contrast to local insolation, Griffiths et al. (2009) suggested that high-latitude oceanic circulation, such as Atlantic meridional overturning circulation, has forced precipitation of the Australian-Indonesian monsoon since the Holocene, which also agrees with $\delta^{18}O$ values from Borneo (Partin

Received September 24, 2021; accepted June 27, 2022

E-mail: liyu@lzu.edu.cn

et al., 2007). Meanwhile, the high-latitudes ocean and atmospheric circulation in the Northern Hemisphere have a predominant effect on the precipitation pattern in middle to high latitudes. In other words, westerlies carry vapor from the North Atlantic and Pacific Oceans to Central Asia and North America (An et al., 2008; Chen et al., 2008; LeGrande and Schmidt, 2009). Effective moisture interpreted from multiple pollen records from Central Asia shows that the middle Holocene is the environmental optimum period at middle latitudes (Chen et al., 2008). Since the late glacial period, along with the rapid decline of the Northern Hemisphere continental ice sheets, the Greenland ice cores indicate a rising temperature in the North Atlantic (Grootes and Stuiver, 1997), consistent with the lake-level change in southern Finland at high latitudes (Heikkilä et al., 2010). However, a paleoclimate database including lake levels, pollen assemblages, and eolian sediment records from Mongolia shows a more southward distribution of forest-steppe environments during the early to middle Holocene (An et al., 2008). Although we have made significant progress in paleoclimate studies using climate proxies, the interpretation of proxy values are still troubling for researchers due to the multiplicity of paleoclimate proxies. The speleothem records from China reveal strong spatial heterogeneity in Holocene moisture evolution between the East Asian and Indian summer monsoon domains, and the $\delta^{18}O$ values of lake sediments sampled from the Shiyang River basin of north-western China suggest asynchronous Holocene Asian monsoon vapor transport and precipitation (Li and Xu, 2016), but other papers determine that $\delta^{18}O$ values help to distinguish the boundary between the Asian monsoon and westerlies on the millennial scale of variability (Chen et al., 2008, 2010). The $\delta^{18}O$ values from the Sajama Mountains (18.1°S, 68.9°W) are good candidates for studying the late Quaternary paleoclimatology of South America when some studies point out that their values represent ice core accumulation or precipitation. However, some studies demonstrate that it closely correlates with NCEP-NCAR 400-500-hPa temperature in a grid box centered at 17.5°S, 70°W on seasonal-to-interannual time scales. Therefore, the correct understanding of the information in paleoclimate proxies is crucial to our understanding of paleoclimate change.

After Joseph introduced the concept of climate models, these models improved our understanding of the mechanisms of climate and its interactions in the last half century (Smagorinsky, 1963). Models are used to understand and explain the El Niño-Southern Oscillation, the relationship between Atlantic Meridional Overturning Circulation and winter temperature patterns over Europe or the globe (Pausata et al., 2017; Zhu et al., 2019; Găinuşă-Bogdan et al., 2020). However, recent studies suggest that climate models simulating precipitation fields are too small compared with those from instrumental (Govindan et al., 2002; Laepple and Huybers, 2014) data and paleoclimate records (Ault et al., 2014; Laepple and Huybers, 2014; Parsons et al., 2017). Instrumental and paleoclimate data indicate that natural hydroclimate tends to be more energetic at low frequencies (Ault et al., 2014), and regional precipitation is underestimated. The precipitation mechanisms related to the greening of the Sahara are far from being properly represented in general circulation models, as most climate models severely underestimate past wet conditions over North Africa (Adam et al., 2019). These models are estimated to require 500-800 mm/yr of precipitation in 20°−25°N for a sustainable greening of the Sahara during the early Holocene (Hopcroft et al., 2017).

Therefore, to enhance our understanding of climate mechanisms while better understanding past climate change, we have developed a preliminary average-probability method that combines the advantages of indicators and models in which precipitation at a grid on the model is used as the independent variable and climate proxy values are used as the dependent variable to quantitatively correct and reconstruct precipitation at a grid. It contains the low-frequency and abrupt change response to past climate changes but also models quantitative changes in precipitation at different spatiotemporal scales. This approach can also improve our understanding of the mechanisms causing the observed climate changes. In this study, we combined the TraCE precipitation model and 349 records to reconstruct global precipitation over the last 12000 years. We used the newest version of the TraCE precipitation data set to explore the thermodynamic and dynamic precipitation mechanisms, thus improving our understanding of past precipitation patterns.

2 Data and methods

2.1 Record selection criteria and chronological framework

Although sedimentary records commonly reveal past changes in environmental and climatic variables, such as vegetation, temperature, and moisture, there is controversy over the interpretation of data records. High-resolution oxygen isotope ($\delta^{18}O$) profiles of speleothems commonly provide a record of Holocene precipitation intensity (Wang et al., 2007; Li and Xu, 2016; Yang et al., 2016; McGee, 2020). Cave $\delta^{18}O$ values reflect the variation in past precipitation remains controversial (Li and Xu, 2016), but in our validation experiment (Supplementary Information Figs. S4−S7), we found a correlation between precipitation and $\delta^{18}O$ values. In contrast, it is commonly accepted that Holocene lake-level records are closely related to precipitation changes, a connection that has been validated by lake deposits and shown by verification studies. According to the results of

our validation experiment and previous studies (see Verification for data section of Supplementary Information), cave deposits and lake sediments provide useful indicators for reconstructing Holocene precipitation.

We used four criteria to select various types of records (such as data on Holocene lakes and speleothems). 1) Records must have a reliable chronology and continuous Holocene sedimentary sequences. 2) Each time series spans at least 6500 years if not the entire Holocene. 3) Indicators from the records data must include direct lake-level changes or precipitation change information. 4) Data are publicly available (such as via PANGAEA or NOAA-Palaeoclimate) or are nonproprietary data available directly from the original authors. According to these criteria, we obtained data from 265 lake sediment samples, 38 cave sediment samples, 36 marine sediment samples, and 10 ice cores (Table 1). We used Calib611 software to calibrate and compile the radiocarbon ages of the lake, pollen, and speleothem records (^{14}C yr BP) by calendar year (cal BP); by such calibration, we removed all possible influences of carbon in the originally provided age data. Our composited indicator includes all available indicators based on lake deposits and oxygen isotope values in all cave sediments (Fig. 1).

2.2 Simulation model

To reconstruct the relationships with simulated effects based on known climatic forcing and records, we selected the TraCE-21ka transient climate model simulations and records from the NOAA data center to establish regression equations. Time-varying insolation, greenhouse gases, ice-sheet topography, land, ocean paleogeography, and meltwater flux to oceans drive the TraCE-21ka transient climate-model simulations for the period 22 cal ka BP to the present. We incorporated TraCE-21ka global precipitation-simulation data as the local precipitation-signal population for choosing the indicators in our study.

2.3 Methods

Indicators qualitatively characterize local precipitation signals very well. However, because local precipitation is affected by local factors, such as topography, lake basin characteristics, groundwater, and melting snow, indicators cannot discern large-scale humidity changes and are effective only for regional or local precipitation. Therefore, we do not have a single record that provides a spatiotemporal precipitation pattern for the global climate system. we rely on models to understand the transformation of precipitation over millennia and on an orbital timescale and at different spatial scales (such as hemispheric or even global). With the help of models, we can understand the main trends and large-scale dynamics of precipitation in the past, but for subtle climate changes, especially as represented by centennial-scale precipitation, we found models to be ineffective for our research. Previous studies show that even the temperature and precipitation trends are found to be locally reliable, which is due to the differing global mean climate response rather than a correct representation of the spatial variability of the climate change signal to date. In addition, research

Table 1 List of data sets used in reconstruction

Site name	Core name	Proxy	Latitude/(°)	Longitude/(°)	Resolution/yr	Reference
Cave of the Bells	COB-01-02	$\delta^{18}O$	31.75	−110.75	50	Wagner et al. (2010)
Botuver Cave	BT2	$\delta^{18}O$	−27.22	−49.16	100	Cruz et al. (2005); Wang et al. (2007)
Buca della Renella	RL4	$\delta^{18}O$	44.00	0.00	56	Drysdale et al. (2006)
Buckeye Creek Cave	BCC-002/BCC-004/BCC-006	$\delta^{18}O$	37.97	−80.4	15	Hardt et al. (2010); Springer et al. (2008)
Cold Air Cave	T7/T8	$\delta^{18}O$	−24.02	29.11	13	Holmgren et al. (2003); Repinski et al. (1999)
Cold Water Cave	CWC-1s/CWC-2ss/CWC-3L	$\delta^{18}O$	43.47	−91.97	17	Denniston et al. (1999a)
Dongge Cave	D4/DA	$\delta^{18}O$	25.28	108.08	5	Dykoski et al. (2005); Wang et al. (2005); Yuan et al. (2004)
Fort Stanton	Fort Stanton	$\delta^{18}O$	33.30	−105.30	33	Asmerom et al. (2010)
Gunung Buda National Park	BA04/SCH02/SSC01	$\delta^{18}O$	4.030	114.80	20	Partin et al. (2007)
Heshang Cave	HS-4	$\delta^{18}O$	30.45	110.416	8	Hu et al. (2008)
Hoti Cave	H5	$\delta^{18}O$	23.08	57.35	5	Neff et al. (2001)
Hulu Cave	H82/MSD/PD/YT	$\delta^{18}O$	32.50	119.16	2	Wang et al. (2001)
Jerusalem West Cave	AF12	$\delta^{18}O$	31.78	35.15	517	Frumkin et al. (1999)
Jiuxian Cave	C996-1/C996-2	$\delta^{18}O$	33.56	109.10	19	Cai et al. (2010)

(*continued*)

Site name	Core name	Proxy	Latitude/ (°)	Longitude/ (°)	Resolution/ yr	Reference
Katerloch Cave	K1/K3	$\delta^{18}O$	47.08	15.55	2	Boch et al. (2009)
Liang Luar Cave	LR06-B1/LR06-B3	$\delta^{18}O$	−8.53	120.43	10	Griffiths et al. (2009)
Lianhua Cave	A1	$\delta^{18}O$	29.48	109.53	8	Cosford et al. (2009)
Lynds Cave	Lynds Cave Core 001	$\delta^{18}O$	−41.58	146.25	73	Xia et al. (2001)
Ma'ale Efrayim Cave	Ma'ale Efrayim Cave Core 001	$\delta^{18}O$	32.08	35.37	371	Vaks et al. (2003)
Moomi Cave	M1-5	$\delta^{18}O$	12.50	54.00	22	Shakun et al. (2007)
Mystery Cave	MC-28	$\delta^{18}O$	43.62	−92.30	70	Denniston et al. (1999b)
NWSI north-west of the South Island	nz-comp-001	$\delta^{18}O$	−42.00	172.00	36	Williams et al. (2010)
Peqiin Cave	Peqiin Cave Core 001	$\delta^{18}O$	32.58	35.19	469	Bar-Matthews et al. (2003)
Pink Panther Cave	PP-1	$\delta^{18}O$	32.083	−105.17	18	Asmerom et al. (2007)
Poleva Cave	PP10	$\delta^{18}O$	44.72	21.75	77	Constantin et al. (2007)
Qunf Cave	Q5	$\delta^{18}O$	17.17	54.30	7	Fleitmann et al. (2007)
Sanbao Cave	SB10/SB26/SB27/SB3/SB43/ SB44/SB49	$\delta^{18}O$	31.67	110.43	13	Dong et al. (2010); Wang et al. (2008)
Sofular Cave	So-1	$\delta^{18}O$	41.42	31.93	7	Fleitmann et al. (2009)
Soreq Cave	Soreq Cave Core 001	$\delta^{18}O$	31.45	35.03	75	Kaufman et al. (2003)
Spring Valley Caverns	SVC-1/2	$\delta^{18}O$	43.75	−92.41	27	Denniston et al. (1999b)
Terciopelo Cave	CT-7	$\delta^{18}O$	10.17	−85.33	4	Lachniet et al. (2009)
Cueva del Tigre Perdido	NC-A/B	$\delta^{18}O$	−5.94	−77.30	23	van Breukelen et al. (2008)
Venado Cave	Venado Cave Core 001	$\delta^{18}O$	10.60	−84.80	15	Lachniet et al. (2004)
Xiangshui Cave	X3	$\delta^{18}O$	25.25	110.92	69	Cosford et al. (2008)
Yamen Cave	Y1	$\delta^{18}O$	25.48	107.90	9	Yang et al. (2010)
Yaoba Don Cave	YB1	$\delta^{18}O$	28.80	109.83	128	Cosford et al. (2008)
Aral sea		$\delta^{18}O$	59.70	44.98		Filippov and Riedel (2009)
Bear lake		$\delta^{13}C$, $\delta^{18}O$, TC, TIC, OC, $CaCO_3$, Ca, Mg, B, Ba, Fe, K, Li, Mn, Na, P, Sr, Ti	−111.33	42.00		Dean et al. (2006)
Chad Lake		$\delta^{18}O$	14.19	13.47		Bouchette et al. (2010)
Eyre Lake		$\delta^{18}O$	137.70	−29.07		Magee et al. (2004)
Great Salt Lake	USGS 96,95	Bulk organics, Humic acid from organic materials, Charcoal	−112.52	41.20	200	Oviatt et al. (2015)
Huguangyan Maar lake		Ti, Fe, Mn, MS., S, TOC, bio.-SiO_2	110.28	21.15		Yancheva et al. (2007)
Laguna Yanacocha		Si, S, K, Ca, Ti, Mn, Fe, Zn, Rb, Sr, Zr	−75.93	−10.56	4	Stansell et al, (2015)
Lake Chichancanab		$\delta^{13}C$, $\delta^{18}O$, $CaCO_3$,S	−88.82	19.87	22	Hodell et al. (1995)
Lake Issyk-Kul	IK97	$\delta^{13}C$, $\delta^{18}O$, Sr/Ca	77.25	42.46	194	Ricketts et al. (2001)
Lake Malawi	M98-1P/M98-1P	BSi, LSR, MAR, BSi MAR	33.83	−13.52	19	Johnson et al. (2002)
Lake Qinghai		brightness, redness	100.30	37.06	32	Ji et al. (2005)
Lake Tanganyika		dD, $\delta^{13}C$, TEX86	29.83	−6.08	185	Tierney et al. (2008)
Lake Titicaca	Titicaca2014dD-LT01-2B	dD	−69.16	−15.94	266	Fornace et al. (2014)
Lake Towuti	TOW9	Al, Mg, K, Ti,Fe, Cr, Co, V, U	121.52	−2.73	624	Costa et al. (2015)
Makgadikgadi Basin	Kal98	U,Th, K	24.70	−20.51		Shaw et al. (2003)
Victoria lake	LV95-1P	TEX86, Leaf Wax, dD , $\delta^{13}C$	33.20	−1.23	209	Berke et al. (2012)

Note: the completed form is in the Supplementary Materials.

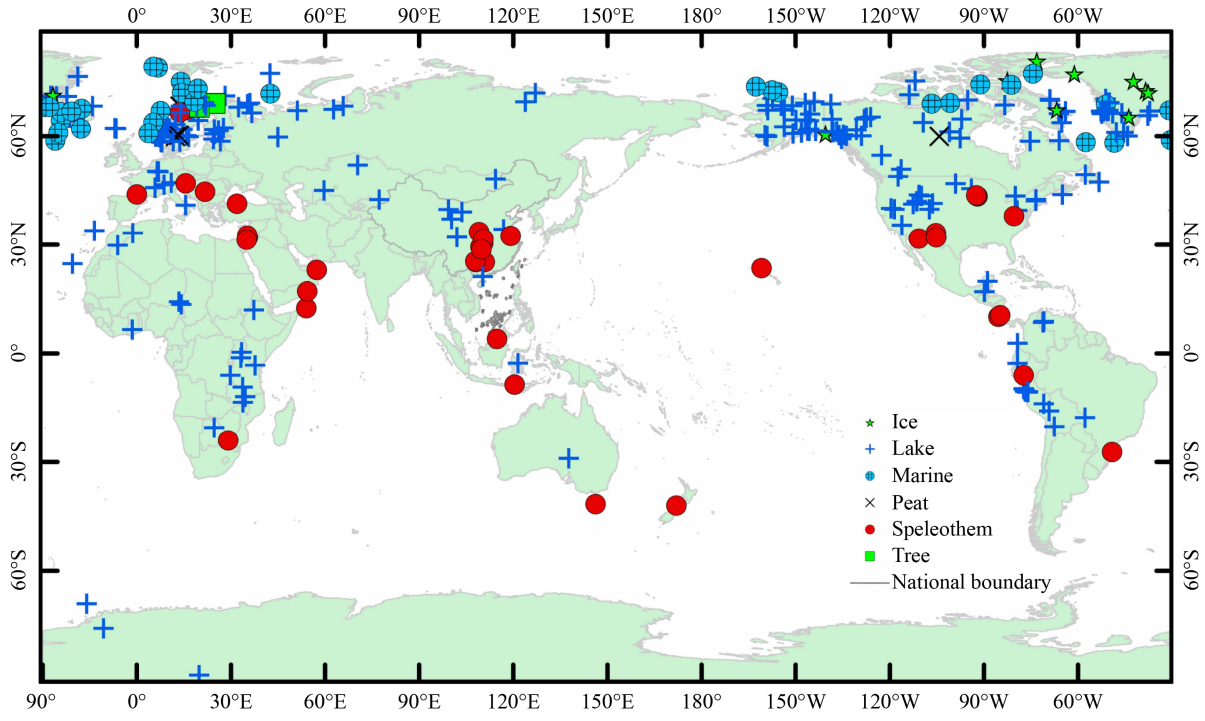

Fig. 1 Location map of proxy precipitation data sets. Map of precipitation data sets from this study with precipitation proxies indentified by color coding.

suggests that the spatial variability in the pattern of warming is too small, and the precipitation trends are also overconfident (Govindan et al., 2002; Ault et al., 2014; Laepple and Huybers, 2014; Adam et al., 2019). Whether the spatial-scale divide between local and regional can be dissolved is an important factor that affects our ability to study large-scale spatiotemporal precipitation changes from millennia to centuries. Thus, we have sought a method to obtain indicators to respond to past centennial-scale climate change on a local level and to attain the model's advantage in continuous, dynamic simulation, at expanded spatiotemporal scales, of past precipitation patterns to enhance our understanding of climate mechanisms and better predict future climate change.

To solve this problem, we developed a preliminary average-probability method, combined with models and records. We first normalized the high-resolution proxy records and model precipitation to make it possible to reflect the climate signal correctly while eliminating the influence of dimension and to ensure that coefficients faithfully reflect weight. Then, the data were interpolated to a 50-yr resolution to avoid the impact of different original data steps on data processing.

We assumed that a large-scale precipitation pattern means that most of the encompassed area has a unified pattern of precipitation. Accordingly, we used the area of lat 0.5° × long 0.5° as the minimum unit for calculating a precipitation time series and as a single precipitation pattern unit to calculate weights. Thus, for large-scale precipitation, we represent presentation type by

$$P_{\mathrm{a}} = XF, \tag{1}$$

where P_{a} is a unit precipitation type for a particular vast area, X is the area weight (coefficient) matrix, and F is the precipitation signal type matrix. Then, for the precipitation sequence of the specific grid I, we formulated an idealized concept as

$$\begin{aligned}&\text{Local Precipitation Signal}\\&= \{D_{Wt}.\text{Distance}, L_{Wt}.\text{longitudetypy},\\&La_{Wt}.\text{latitude} \ldots . A_{Wt}.\text{altitude}\}\,\text{indicator signal}.\end{aligned} \tag{2}$$

We could not quantitatively develop an algorithm to measure so much uncertainty and to determine the weight of various factors in the indicator, so we assumed it would be transformed into a statistical probability of expected questions; this problem to be addressed and be represented as the following:

$$(L - I)^2 = 0, \tag{3}$$

or

$$std(\text{Local Signal} - \text{Indicator Signal}) = 0, \tag{4}$$

where L is the local precipitation signal and I is the indicator signal. If an indicator signal can represent the regional precipitation signal in an accurate and timely manner, then the standard deviation of the two signals is close to zero. Because the population and the sample are finite rather than infinite types, if we collect as many precipitation types as possible, our results are more likely to be accurate. Factors such as the topography, slope

direction, temperature, and evaporation force local precipitation signals, and the resulting factor combination types are limited, leading to a finite number of local precipitation types. We built a sample database to represent the overall idealized types. Our complete set of data samples is based on published or otherwise publicly available data sets. Accordingly, our research problem turned into one focused on probabilities.

As the standard deviation between the two approaches 0, the conversion of such terrain tends to eliminate or reduce the influence of terrain and other factors. Additionally, to avoid cumbersome calculations, we were able to simplify to the following:

$$p = E[(P_o - E[P_o])(I - E[I])] \tag{5}$$

into

$$p = E[P_o I] - E[P_o]E[I]. \tag{6}$$

Using this formula described above, we were unable to incorporate microtopography and other factors into the calculation, thereby we should further shifting it to an issue between local and indicator signals.Additionally, we were unable to grasp the overall appearance of the sample; thus, we introduced the TraCE model, which we assumed could represent millennial-scale precipitation change, thereby representing the sample population. The model has been employed to study glacial periods to discern precipitation change during the last glacial maximum (McGee, 2020) and to predict the orographic effect, greenhouse gases, and thermodynamic and dynamic impacts on Asian-African monsoonal precipitation (Shi and Yan, 2019). All these studies have achieved good results, enhancing our belief in model simulation and prediction capacity.

Meanwhile, we developed a standard data set of indicator types to use in compiling various possible precipitation patterns to best reflect Holocene precipitation types (see Supplementary Materials for details). Accordingly, for the time series at grid point i, indicating a particular precipitation type in the standard data set, Eq. of above can be converted into:

$$P_i = \hat{\mu} + \hat{\beta}X_i + e_i, \tag{7}$$

and therefore

$$e_i = P_i - \hat{\mu} - \hat{\beta}X_i, \tag{8}$$

where e_i is the vector of regression model errors, P_i is the vector of standardized (i.e., zero mean, unit standard deviation) local precipitation at gridpoint i, $\hat{\mu}$ is the matrix vertical displacement deviation, and $\hat{\beta}X_i$ is the weighted score of the local indicator signal. The actual local precipitation signal series used as predictors is related to the scores as the squared-loss function:

$$Q = \sum_{i=1}^{n} e_i^2 = \sum_{i=1}^{n} (P_i - \hat{P}_i)^2 = \sum_{i=1}^{n} (P_i - \hat{\mu} - \hat{\beta}X_i)^2, \tag{9}$$

where e_i is the error of the sample $(P_i - \hat{P}_i)^2$. Then, the line is determined by the Q_{minimum}. That is, $\hat{\mu}$ and $\hat{\beta}$ are determined, and they are regarded as functions of Q, which makes the problem one of seeking an extremum by obtaining a derivative. Then, the partial derivative of Q for the two parameters is estimated by the following:

$$\begin{cases} \dfrac{\partial Q}{\partial \mu} = 2\sum\limits_{i=1}^{n}(P_i - \hat{\mu} - \hat{\beta}X_i)(-1) = 0 \\ \dfrac{\partial Q}{\partial \beta} = 2\sum\limits_{i=1}^{n}(P_i - \hat{\mu} - \hat{\beta}X_i)(-X_i) = 0 \end{cases}. \tag{10}$$

Mathematically, we know that the extremum of the function is the point where the partial derivative is zero, and the equality can be solved as

$$\begin{cases} \hat{\mu} = \dfrac{n\sum X_i P_i - \sum X_i \sum P_i}{n\sum X_i^2 - (\sum X_i)^2} \\ \hat{\beta} = \dfrac{\sum X_i^2 \sum P_i - \sum X_i \sum X_i P_i}{n\sum X_i^2 - (\sum X_i)^2} \end{cases}, \tag{11}$$

and

$$\begin{cases} \hat{\mu} = \dfrac{\sum xP_i - \dfrac{1}{N}\sum x \sum P_i}{\sum x^2 - \dfrac{1}{N}(\sum x)^2} \\ \hat{\beta} = \dfrac{\sum xP_i - \dfrac{1}{N}\sum x \sum P_i}{\sum x^2 - \dfrac{1}{N}(\sum x)^2} \end{cases}. \tag{12}$$

This yields the extreme point of the squared-loss function for the local precipitation signal i from a series of indicators in the data set. For precipitation at grid point i and the data set sequence, we expect that $\hat{\beta}_m$ ($m = 1, 2, 3, \ldots, n$) can infinitely approach one. That is, the sample must conform to the overall distribution, which makes the problem solvable with three variables:

$$\hat{P}_i = \lim_{\hat{\beta}_m \to 1} \hat{\beta}_m X_i + \hat{\mu}_m, \tag{13}$$

where $\hat{P}_i$ is the reconstructed precipitation signal in grid i. That the standard data set likely mixed with other climate signals does not affect our results. Although we used the content of the paper for screening criteria in the process of selecting indicators, we tried to find credible information to show that it can reasonably represent precipitation, but it was still inevitable and unintended that signals representing other climatic factors were intermixed, however, at a limited scope. By our algorithm, if some type of data represented other climatic signals, then their standard deviation with local precipitation is greater than that between the local precipitation signal and the precipitation indicator;

accordingly, even the addition of other climate signals has no real impact. Furthermore, when the standard deviation between other local and indicator signals approaches zero, then the single climate factor directly forces the local precipitation signal and indicator, and our results are not affected.

3 Results

To explore a systematic reconstruction of precipitation, deepening our understanding of the precipitation mechanism and its role in the global hydrologic cycle, we obtained data from 265 lake deposit samples, 38 cave sediment samples, 36 marine sediment samples, and 10 ice cores. We reconstructed millennia-scale precipitation changes according to 12 designated areas (Table 2, Fig. 2). The results show that correlation coefficients between simulated precipitation and records over the past 12000 years were correlated with a 0.99 level (Supplementary Materials Fig. S3), demonstrating that the reconstructions were related to climate modeling precipitation and records.

We found that the precipitation reconstructions at low latitudes (0030NEA; 0030NNAm; 0030NNAf) were in the range of 662−1453 mm/yr, with a maximum value of ~10 cal ka BP, which was matched with 0030SSAm and was the highest precipitation recorded in the 12 reconstructions (Table 3). The precipitation reconstruction values for 3060NEA and 3060NNAm were in the range of 291−480 mm/yr, of which the lowest values were from the early Holocene and the higher values were from the middle to late Holocene. We compared the average precipitation reconstructions in low latitudes against high latitudes, and the results suggest that among the precipitation reconstructions within hemispheres, the most common precipitation in low latitudes was ~1000 mm/yr, whereas the most common precipitation in middle and high latitudes was found to be in the range of 400−500 mm/yr. The reconstructions indicate that precipitation patterns have changed since the early Holocene, whereas low and high values reflect alternating dry-wet cycles on centennial to millennial timescales. Interestingly, the reconstructions also exhibit coherent changes, including a 200-yr cycle that persists throughout the entire reconstructed period in 12 precipitation reconstructions, thereby further revealing that there has been a centennial-scale climate system process forcing precipitation worldwide. The results also reveal three types of precipitation patterns in the 11 continental reconstructions: (I) monsoon precipitation pattern (0030NEA, 0030NNAm, 0030NNAf, 0030SEA, 0030SSAm, and 0030SSAf); (II) westerlies precipitation pattern (3060NEA, 3060NNAm, 6090NEA, and 6090NNAm); and (III) monotonic increasing precipitation pattern (6090SSAA, more detail shown in Table 3). Overall, we found precipitation reconstructions at orbital timescales during the Holocene as reproduced by the average probability method to be trustworthy.

Table 2 Codes of 12 precipitation reconstructions

Latitude[1)]	Area[2)]	Code[3)]
0°–30°N	Eurasia[4)]	0030NEA
0°–30°N	North America	0030NNAm
0°–30°N	North Africa	0030NNAf
0°–30°S	Eurasia	0030SEA
0°–30°S	South America	0030SSAm
0°–30°S	South Africa	0030SSAf
30°N–60°N	Eurasia	3060NEA
30°N–60°N	North America	3060NNAm
60°N–90°N	Eurasia	6090NEA
60°N–90°N	North America	6090NNAm
60°S–90°S	South America and South Africa	6090SSAA
90°S–90°N	Global land	GLP

Notes: 1) Range of area of precipitation. 2) Reconstructed areas, including continental- and global-scale lands. 3) Code representing precipitation on continental land in designated latitude range. 4) The Eurasia includes the Northern Hemisphere part of Australia.

4 Discussion

4.1 Precipitation reconstruction forcing at low latitudes

Our precipitation reconstructions (0030NEA, 0030NNAm, 0030NNAf) are in accord with previous research (Figs. 3(a)−3(c)) in which the monsoon precipitation corresponds with the local summer insolation. The $\delta^{18}O$ values from Holocene sedimentary material sampled in Dongge Cave and high-resolution data records of bulk titanium content in a sediment core from the basin under the Gulf of Cariaco (off Venezuela) reflect the precipitation-evaporation pattern associated with the monsoon system (Haug et al., 2001; Dykoski et al., 2005; Duan et al., 2014). Three reconstructions (0030NEA, 0030NNAm, 0030NNAf) increased during the early Holocene and decreased in the middle and late Holocene. The drop in precipitation during the middle to late Holocene further in our reconstruction (0030NNAf) is consistent with the general trend toward aridity in North Africa, the result of the intensification of the African monsoon (deMenocal et al., 2000). Meanwhile, we also noticed a more dramatic oscillation in the reconstruction than terrigenous from the African monsoon in the early and middle Holocene dynamic switch (Fig. 3(c)), as well as the same feature in Asian monsoon and North American monsoon precipitation (0030NEA, 0030NNAm, Figs. 3(a)−3(d)). For the North African monsoon, it takes time for changes in moisture

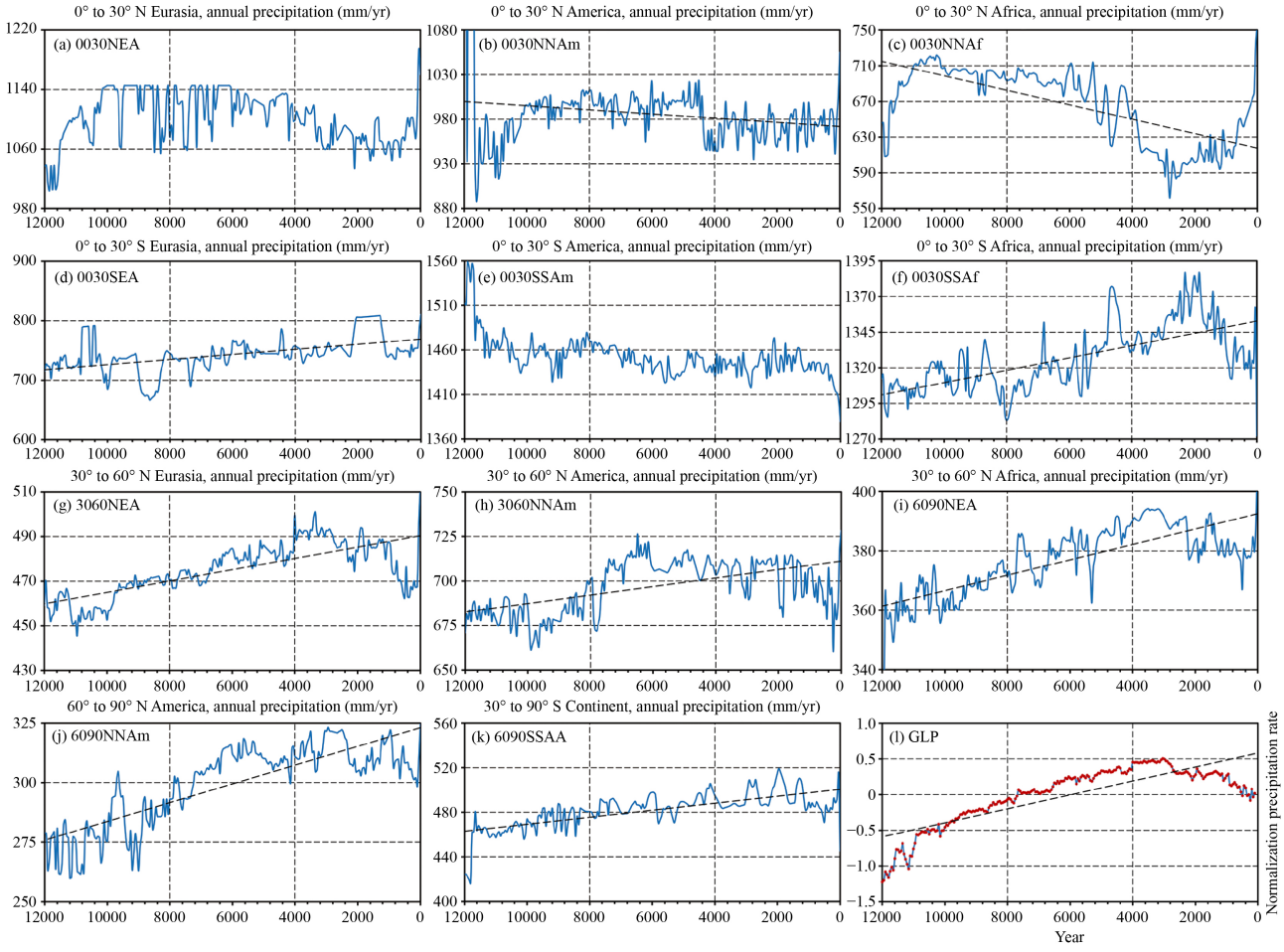

Fig. 2 The Holocene precipitation reconstructions in (a) 0030NEA, (b) 0030NNAm, (c) 0030NNAf, (d) 0030SEA, (e) 0030SSAm, (f) 0030SSAf, (g) 3060NEA, (h) 3060NNAm, (i) 6090NEA, (j) 6090NNAm, (k) 6090SSAA, and (l) GLP (normalization), and the horizontal axis representing the calendar year against the annual precipitation.

Table 3 Statistical description of data

Code	Maximum/(mm·yr^{-1})		Minimum/(mm·yr^{-1})		Mean value of different period/(mm·yr^{-1})				Cycle/yr
	Calender year	Value	Calender year	Value	Total	Early-Holocene	Mid-Holocene	Late-Holocene	
0030N EA	7859	1234.81	2245	1014.07	1133.57	1150.26	1157.08	1089.38	215
0030N NAm	6017	1022.5	11642	888.75	976.25	971.79	989.75	969.86	258
0030N NAf	10352	720.833	2847	565.833	662.24	685.94	665.38	616.46	289
0030S EA	1811	807.407	8611	666.667	740.45	721.36	744.81	755.19	408
0030S SAm	11835	1556.72	94	1404.26	1453.64	1471.85	1444.57	1443.10	330
0030S SAf	1833	1387.71	7976	1285.63	1331.14	1307.05	1331.51	1347.39	255
3060N EA	3473	501.646	11017	446.203	476.86	465.55	483.04	483.59	380
3060N NAm	3473	501.646	11017	446.203	476.86	465.55	483.04	484.25	380
6090N EA	3482	394.568	11952	340	372.13	364.98	379.19	385.09	440
6090N NAm	3011	324.063	11176	259.063	291.75	278.57	311.25	310.71	455
6090S SAA	2023	522.667	11788	417.333	480.17	467.29	487.63	497.04	346

Notes: The maximum/minimum column gives the maximum or minimum value of different reconstruction regions over the reconstructed period. The mean value column shows the mean precipitation values over the total, Early-, Mid-, or Late-Holocene. The cycle column represents the average centennial-scale cycle in 12 precipitation reconstructed regions.

conditions to lead to vegetation change, resulting in changes in the amount of material input offshore. North American monsoon precipitation (0030NNAm) has a larger change in precipitation than Ti (%) for a sudden climate change event at approximately 4.2 cal ka BP. Hopcroft (Hopcroft et al., 2017) suggests that 500−800 mm/yr is the value of precipitation required to maintain a green Sahara in the early Holocene, which coincides with our reconstruction (600−720 mm/yr, Table 3, 0030NNAf). Previous studies prefer a good relationship between monsoon precipitation and local summer insolation at low latitudes, but there is growing evidence that sea-air interactions are the forcing mechanism that determines Australian-Indonesian monsoon precipitation patterns (Griffiths et al., 2009). Our reconstructions (0030SEA) agree with the $\delta^{18}O$ data from Borneo (Majewski et al., 2018), but there are some noteworthy points. The reconstruction (0030SEA) and $\delta^{18}O$ values from Borneo indicate the absence of a Younger Dryas signal compared with the other monsoons, such as the Asia summer monsoon and African monsoon (Figs. 3(a) and 3(b)). A possible explanation for this pheromone is related to the location of the Australian-Indonesian monsoon. The Asian summer monsoon and the African monsoon are at the edge of the subtropical high pressure and Atlantic Meridional Overturning Circulation, therefore, are more sensitive to their meridional upward changes than the Australian-Indonesian monsoon.

4.2 Precipitation reconstructions at middle and high latitudes in the Northern Hemisphere

The westerlies and high-latitude (polar) air mass regulate the middle- and high-latitude precipitation patterns (Wang et al., 2007; Jia et al., 2019). Water vapor from the North Atlantic and Pacific Oceans dominates moisture in Central Asia and North America (Chen et al., 2008; LeGrande and Schmidt, 2009). Precipitation reconstructions (3060NEA, 3060NNAm, 6090NEA, 6090NNAm) in middle latitudes indicate lower precipitation during the early Holocene before a maximum of ~2 cal ka BP, after which it yields stable semiarid conditions with moderate precipitation. This is consistent with the Holocene effective humidity variation reconstructed based on multiproxy approaches. Studies by Chen et al. (2006, 2008, 2010, 2019) show that during the middle to late Holocene, moisture conditions are enhanced with the change in position of the westerlies and the increase in water vapor, runoff, and precipitation (Fig. 3(f)). However, the palaeoprecipitation estimates for the middle latitudes of Asia are mismatched with the effective moisture at the change scale. The moisture scale values,

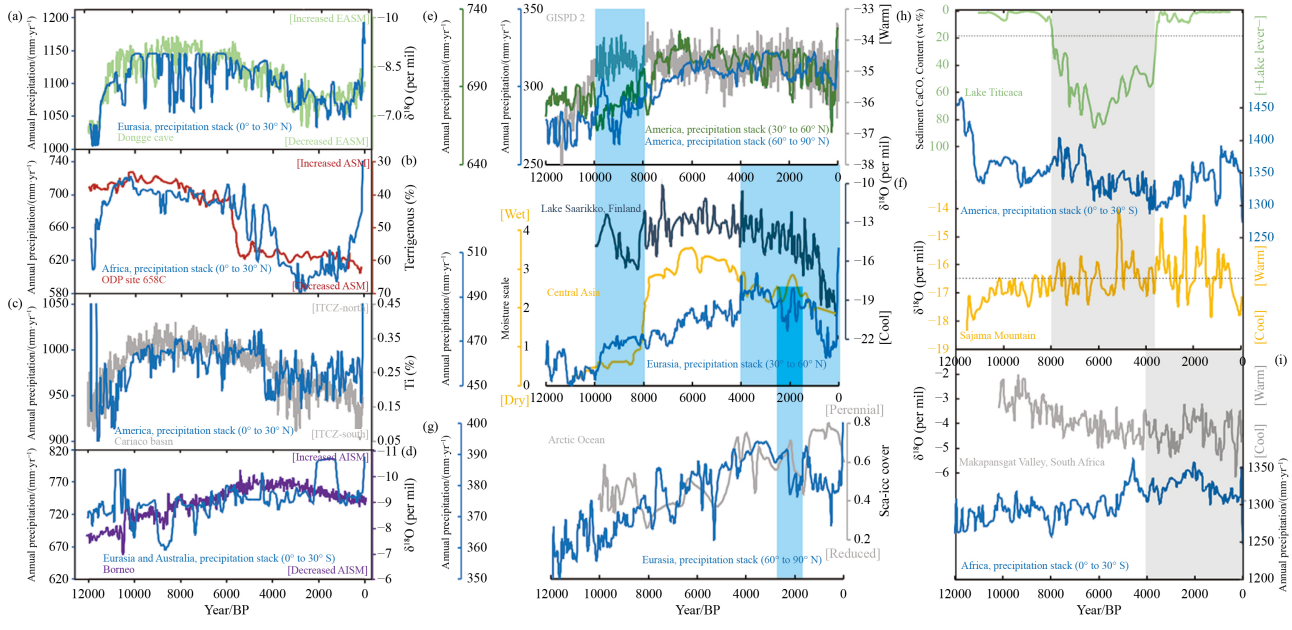

Fig. 3 Comparison of Holocene precipitation reconstructions and paleoclimate records. (a) to (d) Zonal mean precipitation reconstructions for monsoon latitude bands from this study are compared to the speleothem (Dykoski et al., 2005; Partin et al., 2007; Duan et al., 2014). Terrigenous (deMenocal et al., 2000) and Ti data (Haug et al., 2001), which are proxies for precipitation and local temperature; EASM, East Asian Summer Monsoon; AISM, Australian-Indonesian Summer Monsoon. ASM, African Summer Monsoon. (e) to (g) Zonal mean precipitation reconstructions for middle- and high-latitude bands from this study are compared to ice cores (Grootes and Stuiver, 1997), interpreted from pollen data moisture scales (Chen et al., 2008), sediment isotopes (Heikkilä et al., 2010) and sea ice cover (Stein et al., 2017a; Stein et al., 2017b). (h) to (i) Zonal mean precipitation reconstructions for Southern Hemisphere latitude bands from this study are compared to speleothem (Hardy et al., 2003; Holmgren et al., 2003) and lake $CaCO_3$ contents (Fritz et al., 2006).

which are close to 0 until ~8.0 cal ka BP, experience a sharp increase compared to the gentle change in precipitation reconstruction. Because the effective moisture is deduced from vegetation conditions, the abrupt change in its value is due to the accumulation of local vegetation conditions. We know that the northern boundary of the Asian monsoon reaches as far as the Shiyang River (39°03′N, 103°40′E; Li and Xu, 2016), but precipitation reconstruction is based on the weighted average of its share of the grids in the climate model; therefore, the signal of the monsoon in middle latitudes is not obvious. Lake levels, pollen assemblages, and eolian sediment records from Mongolia suggest a more southward distribution of forest-steppe environments during the early and middle Holocene, enhancing aridity in the middle Holocene and increasing humidity in the late Holocene (An et al., 2008). This finding opposes our reconstructions, showing that in addition to the zonal effect, the meridional effect also plays a key role in the middle- to high-latitude moisture and vegetation change. The ice sheet at high latitudes shift the ocean circulation and atmospheric circulation more southward (northward) in the early Holocene, along with the rapid incline (decline) of the Northern Hemisphere continental ice sheets (Grootes and Stuiver, 1997). The middle- and high-latitude precipitation reconstruction occurrence from 12.0 cal ka BP onward is in accordance with other evidence of the onset and characteristics in southern Finland (Heikkilä et al., 2010), suggesting coupled changes between precipitation and temperature at middle and high latitudes (Figs. 3(e)−3(g)).

4.3 Precipitation reconstructions of South America and Africa in the Southern Hemisphere

Precipitation reconstructions (0030SSAm, 0030SSAf) for South America and Africa in the Southern Hemisphere during the Holocene are illustrated in Figs. 3(h) and 3(i). Reconstructions during the Holocene were similar to the high-frequency signals of local indicators such as Sajama Mountain (Hardy et al., 2003), but the low-frequency signals were reflected at different scales (Figs. 3(h) and 3(i)). The high lake level of Lake Titicaca is manifested in the early and late Holocene (Fritz et al., 2006), while the reconstructed precipitation experienced a sharp decrease in precipitation in the early Holocene and an increase in precipitation in the late Holocene. Reconstruction (0030SSAf) represents and from antiphase change with the temperature change of the Makapansgat Valley, South Africa. The $\delta^{18}O$ values from the Makapansgat Valley are consistent with reconstruction (Fig. 3(i)) on the high-frequency signal but antiphase on the millennial scale (Holmgren et al., 2003). However, the length of the Makapansgat Valley sample records South African climate change in the last 25.0 cal ka BP, while its growth halted during the period from ~14−~10 cal ka BP. The oxygen and carbon isotopes (−3.2‰ and −6.5‰) are positively correlated between 25 and ~13 cal ka BP, while they are negatively correlated between ~10 cal ka BP until recently, meaning that our results are consistent with Makapansgat Valley carbon isotopes between 12.0 and 0 cal ka BP. It also concluded that $\delta^{18}O$ value shifts in rain implied considerable overprinting of the temperature-dependent fractionation from seepage water to carbonate (Holmgren et al., 2003). Meanwhile, the pollen from the Tswaing Crater shows that its open dry thornveld became wetter at 30−7 cal ka BP and sustainable with warm broad-leaf woodland and a local swamp paleoenvironment at 7−3.5 cal ka BP (Scott, 1999). Lake level records from Africa indicate that widespread aridity did not occur until after 5.0 cal ka BP (Gasse, 2000). Thus, a higher abundance of $\delta^{18}O$ values in the stalagmite indicates the prevalence of stronger evaporation but not necessarily low precipitation. In addition, an increasing amount of evidence indicates that the precipitation in South America and the Southern Hemisphere part of Africa is in accordance with the Northern Hemisphere summer insolation. Pollen-inferred precipitation from the African mountains near the equator (3°26′ and 3°55′S) shows that that area reaches the maximum (600 mm/yr) at 8.0 cal ka BP, and the drier signal of low precipitation is expressed post-4 cal ka BP (Bonnefille and Chalie, 2000). Considering that Africa and South America have less land area in the 60°S−90°S range and few records we collected for these latitudes, although those reconstructions are given in the results, we have not addressed this precipitation reconstruction (6090 SSAA) here.

4.4 Estimating the high- and low-frequency signal in reconstructions

Reconstruction of precipitation and long-timescale records demonstrate the interaction between Milankovitch forcing and the influence of local components originating from the global thermohaline system (Figs. 3(a)−3(i), Fig. 4). Figure 4 reflects the reconstruction (GLP) close correspondence to the temperature trend in $\delta^{18}O$ values from the GISP2 ice core in Greenland (Grootes and Stuiver, 1997), and we observed excellent replication of weak events between most precipitation reconstructions and records (Figs. 3(a)−3(i), Fig. 4). These events are possibly linked to Holocene ice-rafting events in the North Atlantic. The $\delta^{18}O$ values from GISP2 represent the change in North Atlantic temperature, which serves to redistribute heat according to the state of the Atlantic Meridional Overturning Circulation, in concert with the meridional movement of the Intertropical Convergence Zone on a sudden millennial scale (Holmgren et al., 2003; Stocker and Johnsen, 2003; Griffiths et al., 2009). In

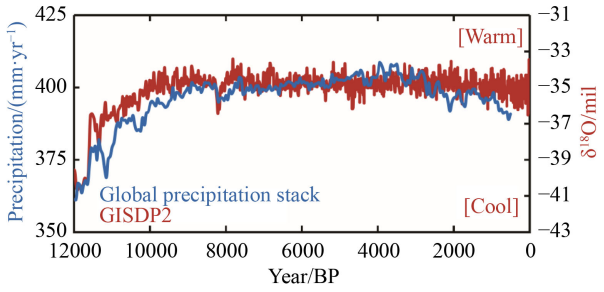

Fig. 4 Global precipitation reconstruction stack and $\delta^{18}O$ at GISDP2 plotted against calendar year.

contrast, the Australian-Indonesian monsoon and precipitation reconstruction (0030SEA) does not record a significant 8.2 ka event. Climate change in the South Hemisphere part of Africa and America shows a continuous wetting trend, with significant cooling events now showing any interruption to this trend (Figs. 3(h) and 3(i)). Instrumental and paleoclimate data indicate that natural hydroclimate fluctuations tend to be more energetic at high frequencies than climate models, and regional precipitation discrepancies remain unresolved in climate models (Ault et al., 2014). Research by Adam et al. (2019) show that the mechanisms related to the greening of the Sahara, as with most climate models, severely underestimate past wet conditions over North Africa (Adam et al., 2019). However, the estimated hydrological changes are not reproduced in the climate model simulations, which require 500−800 mm/yr of rainfall in the 20°N−25°N range to maintain a green Sahara, but it is consistent with our reconstruction (Hopcroft et al., 2017). According to our results and modeling experiments, a critical element for successfully simulating the energy of high-frequency signals depends on the initial conditions of the deep ocean state (Zhu et al., 2019). We also need to see growing evidence from records pointing out synchronous evolutionary trends between the two hemispheres in Africa. Pollen-inferred precipitation from equatorial mountains in Africa (3°26′S and 3°55′S) reaches the maximum (600 mm/yr) at 8 cal ka BP, and great variations between low and high precipitation values are expressed in the last 4 cal ka BP (Bonnefille and Chalie, 2000), which is not shown in our reconstructions. Bearing in mind the large uncertainties for the reconstructions, we use the precipitation variables of the model as independent variables to select indicators to correct the precipitation of the model at a given grid. Thus, this precipitation reconstruction of the Southern Hemisphere (Fig. 3(i)) has similar characteristics to the model. In addition, our reconstruction reproduces the main signal of the Australian-Indonesian monsoon (Fig. 3(d), 0030SEA); even the sub-monsoon region of Australian-Indonesian has less land area and fewer land-based indicators, but reconstruction is not smooth at ~2−~1.5 cal ka BP. The same feature is true for the low latitude Asian monsoon reconstruction (Fig. 3(a), 0030NEA) at ~ 9.0, ~ 7.8, and ~ 6.0 cal ka BP, even though it passed the robust test (Supplementary Materials Fig. S2).

5 Conclusions

In this paper, we developed a new approach to integrating data from 265 lake deposit samples, 38 cave sediment samples, 36 marine sediment samples, and 10 ice cores with a paleoclimate model to reconstruct precipitation during the last 12000 years.

To study the spatiotemporal precipitation variations in Asia, Africa, America, and Europe at different locations, we developed a preliminary average probability method. We found that Holocene global precipitation is divided into two main types - the monsoon precipitation pattern in the low latitudes and the westerlies precipitation pattern in the middle to high latitudes, and there are different degrees of decreasing precipitation in the late Holocene except for South America and the South African region.

During the same period, the total amount of precipitation decreased from 1000 to 300 mm/yr in the low to high latitudes. Additionally, all the reconstructed precipitation types have similar precipitation cycles at the centennial and millennial scales, indicating that the insolation, ocean circulation, and atmospheric circulation in the Northern Hemisphere play a key role in the precipitation cycle, showing that the climate system is a teleconnection and complex system.

The westerlies and monsoon system patterns of precipitation reconstructions in the two hemispheres reveal general late-Holocene aridity, with peak humidity at 3.0−3.5 cal ka BP in the westerlies precipitation pattern and apex aridity at ~2.0 cal ka BP in the monsoon precipitation pattern.

Our reconstructions provide some useful attempts to resolve the challenges of models at low frequencies and aptitudes; however, the majority of these results were obtained through different proxy records from separate materials with distinct resolutions and dating uncertainties. Detailed knowledge of the precursors and lags of climate change between oceanic and terrestrial regions connecting low and high latitudes remains controversial (Lea et al., 2000; Xu et al., 2013). Promoting the resolution of records and deep ocean modeling capability remains an important means to improve our understanding of past climate change (Zhu et al., 2019).

Acknowledgement This research was supported by the National Natural Science Foundation of China (Grant No. 42077415); the Second Tibetan Plateau Scientific Expedition and Research Program (STEP) (Grant No. 2019QZKK0202); the Strategic Priority Research Program of Chinese Academy of Sciences (Grant No. XDA20100102); the 111 Project (BP0618001).

Supplementary Materials are available in the online version of this article at https://doi.org/10.1007/s11707-022-1047-5 and are accessible for authorized users.

References

Abram N J, Mcgregor H V, Tierney J E, Evans M N, Mckay N P, Kaufman D S, Thirumalai K, Martrat B, Goosse H, Phipps S J, Steig E J, Kilbourne K H, Saenger C P, Zinke J, Leduc G, Addison J A, Mortyn P G, Seidenkrantz M, Sicre M, Selvaraj K, Filipsson H L, Neukom R, Gergis J, Curran M A J, Gunten L V (2016). Early onset of industrial-era warming across the oceans and continents. Nature, 536(7617): 411–418

Adam O, Schneider T, Enzel Y, Quade J (2019). Both differential and equatorial heating contributed to African monsoon variations during the mid-Holocene. Earth Planet Sci Lett, 522: 20–29

An C B, Chen F H, Barton L (2008). Holocene environmental changes in Mongolia: a review. Global Planet Change, 63(4): 283–289

Asmerom Y, Polyak V J, Burns S J (2010). Variable winter moisture in the southwestern United States linked to rapid glacial climate shifts. Nat Geosci, 3(2): 114–117

Ault T R, Cole J E, Overpeck J T, Pederson G T, Meko D M (2014). Assessing the risk of persistent drought using climate model simulations and paleoclimate data. J Clim, 27(20): 7529–7549

Bar-Matthews M, Ayalon A, Gilmour M, Matthews A, Hawkesworth CJ (2003). Sea-land oxygen isotopic relationships from planktonic foraminifera and speleothems in the Eastern Mediterranean region and their implication for paleorainfall during interglacial intervals. Geochim Cosmochim Acta, 67(17): 3181–3199

Berke M A, Johnson T C, Werne J P, Grice K, Schouten S, Damste J (2012). Molecular records of climate variability and vegetation response since the Late Pleistocene in the Lake Victoria basin, East Africa. Quat Sci Rev, 55: 59–74

Boch R, Spötl C, Kramers J (2009). High-resolution isotope records of early Holocene rapid climate change from two coeval stalagmites of Katerloch Cave, Austria. Quat Sci Rev, 28(23):2527–2538

Bonnefille R, Chalie F (2000). Pollen-inferred precipitation time-series from equatorial mountains, Africa, the last 40 kyr BP. Global Planet Change, 26(1–3): 25–50

Bouchette F, Schuster M, Ghienne J F, Denamiel C, Roquin C, Moussa A, Marsaleix P, Duringer P (2010). Hydrodynamics in Holocene Lake Mega-Chad. Quat Res, 73(2): 226–236

Cai Y, Tan L, Cheng H, An Z, Edwards R L, Kelly M J, Kong X, Wang X (2010). The variation of summer monsoon precipitation in central China since the last deglaciation. Earth Planet Sci Lett, 291(1–4): 21–31

Chen F H, Chen J H, Holmes J, Boomer I, Austin P, Gates J B, Wang N L, Brooks S J, Zhang J W (2010). Moisture changes over the last millennium in arid central Asia: a review, synthesis and comparison with monsoon region. Quat Sci Rev, 29(7–8): 1055–1068

Chen F H, Cheng B, Zhao Y, Zhu Y, Madsen D B (2006). Holocene environmental change inferred from a high-resolution pollen record, Lake Zhuyeze, arid China. Holocene, 16(5): 675–684

Chen F H, Yu Z C, Yang M L, Ito E, Wang S M, Madsen D B, Huang X Z, Zhao Y, Sato T, Birks H J B, Boomer I, Chen J H, An C B, Wünnemann B (2008). Holocene moisture evolution in arid central Asia and its out-of-phase relationship with Asian monsoon history. Quat Sci Rev, 27(3–4): 351–364

Chen F, Chen J, Huang W, Chen S, Huang X, Jin L, Jia J, Zhang X, An C, Zhang J, Zhao Y, Yu Z, Zhang R, Liu J, Zhou A, Feng S (2019). Westerlies Asia and monsoonal Asia: spatiotemporal differences in climate change and possible mechanisms on decadal to sub-orbital timescales. Earth Sci Rev, 192: 337–354

Constantin S, Bojar A, Lauritzen S, Lundberg J (2007). Holocene and Late Pleistocene climate in the sub-Mediterranean continental environment: a speleothem record from Poleva Cave (Southern Carpathians, Romania). Palaeogeogr, Palaeoclimatol, Palaeoecol, 243(3): 322–338

Cosford J, Qing H, Mattey D, Eglington B, Zhang M (2009). Climatic and local effects on stalagmite δ13C values at Lianhua Cave, China. Palaeogeogr, Palaeoclimatol, Palaeoecol, 280(1): 235–244

Cosford J, Qing H, Yuan D, Zhang M, Holmden C, Patterson W, Hai C (2008). Millennial-scale variability in the Asian monsoon: evidence from oxygen isotope records from stalagmites in southeastern China. Palaeogeogr, Palaeoclimatol, Palaeoecol, 266(1): 3–12

Costa K M, Russell J M, Vogel H, Bijaksana S (2015). Hydrological connectivity and mixing of Lake Towuti, Indonesia in response to paleoclimatic changes over the last 60,000 years. Palaeogeogr Palaeoclimatol Palaeoecol, 417: 467–475

Cruz F W, Burns S J, Karmann I, Sharp W D, Vuille M, Cardoso A O, Ferrari J A, Silva Dias P L, Viana O (2005). Insolation-driven changes in atmospheric circulation over the past 116,000 years in subtropical Brazil. Nature, 434(7029): 63–66

Dean W, Rosenbaum J, Skipp G, Colman S, Forester R, Liu A, Simmons K, Bischoff J (2006). Unusual Holocene and late Pleistocene carbonate sedimentation in Bear Lake, Utah and Idaho, USA. Sediment Geol, 185: 93–112

deMenocal P, Ortiz J, Guilderson T, Adkins J, Sarnthein M, Baker L, Yarusinsky M (2000). Abrupt onset and termination of the African Humid Period: rapid climate responses to gradual insolation forcing. Quat Sci Rev, 19(1–5): 347–361

Denniston R F, González L A, Asmerom Y, Baker RG, Reagan MK, Bettis EAI (1999a). Evidence for increased cool season moisture during the middle Holocene. Geology, 27(9): 815–818

Denniston R F, González L A, Baker R G, Asmerom Y, Reagan M K, Edwards R L, Alexander E C (1999b). Speleothem evidence for Holocene fluctuations of the prairie-forest ecotone, north-central USA. The Holocene, 9(6): 671–676

Dong J G, Wang Y J, Cheng H, Hardt B, Edwards R L, Kong X G, Wu J Y, Chen S T, Liu D B, Jiang X Y, Zhao K (2010). A high-resolution stalagmite record of the Holocene East Asian monsoon from Mt Shennongjia, central China. Holocene, 20(2): 257–264

Drysdale R, Zanchetta G, Hellstrom J, Maas R, Fallick A E, Pickett M, Cartwright I, Piccini L (2006). Late Holocene drought responsible for the collapse of Old World civilizations is recorded in an Italian flowstone. Geology, 34: 101–104

Duan F, Wang Y, Shen C C, Wang Y, Cheng H, Wu C C, Hu H M, Kong X, Liu D, Zhao K (2014). Evidence for solar cycles in a late Holocene speleothem record from Dongge Cave, China. Sci Rep, 4(1): 5159

Dykoski C A, Edwards R L, Cheng H, Yuan D X, Cai Y J, Zhang M L, Lin Y S, Qing J M, An Z S, Revenaugh J (2005). A high-resolution, absolute-dated Holocene and deglacial Asian monsoon record from Dongge Cave, China. Earth Planet Sci Lett, 233(1–2): 71–86

Filippov A, Riedel F (2009). The late Holocene mollusc fauna of the Aral Sea and its biogeographical and ecological interpretation. Limnologica, 39(1): 67–85

Fleitmann D, Burns SJ, Mangini A, Mudelsee M, Kramers J, Villa I, Neff U, Al-Subbary AA, Buettner A, Hippler D, Matter A (2007). Holocene ITCZ and Indian monsoon dynamics recorded in stalagmites from Oman and Yemen (Socotra). Quat Sci Rev, 26(1): 170–188

Fleitmann D, Cheng H, Braun-Badertscher S, Edwards R, Mudelsee M, Göktürk OM, Fankhauser A, Pickering R, Raible C, Matter A, Kramers J, Tuysuz O (2009). Timing and climatic impact of Greenland interstadials recorded in stalagmites from northern Turkey. Geophys Res Lett, 36

Fornace K L, Hughen K A, Shanahan T M, Fritz S C, Baker P A, Sylva S P (2014). A 60,000-year record of hydrologic variability in the Central Andes from the hydrogen isotopic composition of leaf waxes in Lake Titicaca sediments. Earth Planet Sci Lett, 408: 263–271

Fritz S C, Baker P A, Tapia P, Garland J (2006). Spatial and temporal variation in cores from Lake Titicaca, Bolivia/Peru during the last 13,000yrs. Quat Int, 158(1): 23–29

Frumkin A, Ford DC, Schwarcz HP (1999). Continental oxygen isotopic record of the last 170,000 years in Jerusalem. Quat Res, 51(3): 317–372

Gagen M H, Zorita E, McCarroll D, Zahn M, Young G H F, Robertson I (2016). North Atlantic summer storm tracks over Europe dominated by internal variability over the past millennium. Nat Geosci, 9: 630–625

Găinuşă-Bogdan A, Swingedouw D, Yiou P, Cattiaux J, Codron F, Michel S (2020). AMOC and summer sea ice as key drivers of the spread in mid-holocene winter temperature patterns over Europe in PMIP3 models. Global Planet Change, 184: 103055

Gasse F (2000). Hydrological changes in the African tropics since the Last Glacial Maximum. Quat Sci Rev, 19(1–5): 189–211

Govindan R B, Vyushin D, Bunde A, Brenner S, Havlin S, Schellnhuber H J (2002). Global climate models violate scaling of the observed atmospheric variability. Phys Rev Lett, 89(2): 028501

Griffiths M L, Drysdale R N, Gagan M K, Zhao J X, Ayliffe L K, Hellstrom J C, Hantoro W S, Frisia S, Feng Y X, Cartwright I, Pierre E S, Fischer M J, Suwargadi B W (2009). Increasing Australian-Indonesian monsoon rainfall linked to early Holocene sea-level rise. Nat Geosci, 2(9): 636–639

Grootes P M, Stuiver M (1997). Oxygen 18/16 variability in Greenland snow and ice with 10^{-3}- to 10^{5}-year time resolution. J Geophys Res, 102(C12): 26455–26470

Hardt B, Rowe H D, Springer G S, Cheng H, Edwards R L (2010). The seasonality of east central North American precipitation based on three coeval Holocene speleothems from southern West Virginia. Earth Planet Sci Lett, 295(3–4): 342–348

Hardy D R, Vuille M, Bradley R S (2003). Variability of snow accumulation and isotopic composition on Nevado Sajama, Bolivia. J Geophys Res-Atmosph, 108(D22): 2003JD003623

Haug G H, Hughen K A, Sigman D M, Peterson L C, Röhl U (2001). Southward migration of the intertropical convergence zone through the Holocene. Science, 293(5533): 1304–1308

Heikkilä M, Edwards TW D, Seppä H, Sonninen E (2010). Sediment isotope tracers from Lake Saarikko, Finland, and implications for Holocene hydroclimatology. Quat Sci Rev, 29(17–18): 2146–2160

Hodell D, Curtis J, Brenner M (1995). Possible Role of Climate in the Collapse of Classic Maya Civilization. Nature, 375: 391–394

Holmgren K, Lee-Thorp J A, Cooper G R J, Lundblad K, Partridge T C, Scott L, Sithaldeen R, Talma A S, Tyson P D (2003). Persistent millennial-scale climatic variability over the past 25,000 years in Southern Africa. Quat Sci Rev, 22(21–22): 2311–2326

Hopcroft P O, Valdes P J, Harper A B, Beerling D J (2017). Multi vegetation model evaluation of the Green Sahara climate regime. Geophys Res Lett, 44(13): 6804–6813

Hu C, Henderson G, Huang J, Zhenghong C, Kathleen J (2008). Report of a three-year monitoring programme at Heshang Cave, Central China. Int J Speleol, 37

Ji J, Shen J, Balsam W, Chen J, Liu L, Liu X (2005). Asian monsoon oscillations in the northeastern Qinghai–Tibet Plateau since the late glacial as interpreted from visible reflectance of Qinghai Lake sediments. Earth Planet Sci Lett, 233(1): 61–70

Jia Y H, Li D W, Yu M, Zhao X C, Xiang R, Li G X, Zhang H L, Zhao M X (2019). High- and low-latitude forcing on the south Yellow Sea surface water temperature variations during the Holocene. Global Planet Change, 182: 103025

Johnson T C, Brown E T, McManus J, Barry S, Barker P, Gasse F (2002). A high-resolution paleoclimate record spanning the past 25000 Years in southern East Africa. Science, 296(5565): 113–132

Kaufman A, Bar-Matthews M, Ayalon A, Carmi I (2003). The vadose flow above Soreq Cave, Israel: a tritium study of the cave waters. J Hydrol (Amst), 273(1): 155–163

Lachniet M S, Asmerom Y, Burns S J, Patterson W P, Polyak V J, Seltzer G O (2004). Tropical response to the 8200 yr B.P. cold event? Speleothem isotopes indicate a weakened early Holocene monsoon in Costa Rica. Geology, 32(11): 957–960

Lachniet MS, Johnson L, Asmerom Y, Burns SJ, Polyak V, Patterson WP, Burt L, Azouz A (2009). Late Quaternary moisture export across Central America and to Greenland: evidence for tropical rainfall variability from Costa Rican stalagmites. Quat Sci Rev, 28(27): 3348–3360

Laepple T, Huybers P (2014). Ocean surface temperature variability: large model-data differences at decadal and longer periods. Proc Natl Acad Sci USA, 111(47): 16682–16687

Lea D W, Pak D K, Spero H J (2000). Climate impact of late Quaternary equatorial pacific sea surface temperature variations. Science, 289(5485): 1719–1724

LeGrande A N, Schmidt G A (2009). Sources of Holocene variability of oxygen isotopes in paleoclimate archives. Clim Past, 5(3): 441–455

Li Y, Wang N, Cheng H, Long H, Zhao Q (2009). Holocene environmental change in the marginal area of the Asian monsoon: a record from Zhuye Lake, NW China. Boreas, 38(2): 349–361

Li Y, Wang N, Zhou X, Zhang C, Wang Y (2014). Synchronous or

asynchronous Holocene Indian and East Asian summer monsoon evolution: a synthesis on Holocene Asian summer monsoon simulations, records and modern monsoon indices. Global Planet Change, 116(5): 30–40

Li Y, Xu L M (2016). Asynchronous Holocene Asian monsoon vapor transport and precipitation. Palaeogeogr Palaeoclimatol Palaeoecol, 461: 195–200

Li Y, Xu L, Zhang C, Liu Y, Zhu G, Zhou X (2018). Temporal and spatial evolution of Holocene vegetation and lake hydrological status, China. Holocene, 28(5): 706–720

Magee J W, Miller G H, Spooner N A, Questiaux D (2004). Continuous 150 k.y. monsoon record from Lake Eyre, Australia: Insolation-forcing implications and unexpected Holocene failure. Geology, 32(10): 885–888

Majewski J M, Switzer A D, Meltzner A J, Parham P R, Horton B P, Bradley S L, Pile J, Chiang H W, Wang X F, Ng C T, Tanzil J, Muller M, Mujahid A (2018). Holocene relative sea-level records from coral microatolls in Western Borneo, South China Sea. Holocene, 28(9): 1431–1442

McGee D (2020). Glacial-interglacial precipitation changes. Annu Rev Mar Sci, 12(1): 525–557

Neff U, Burns SJ, Mangini A, Mudelsee M, Fleitmann D, Matter A (2001). Strong coherence between solar variability and the monsoon in Oman between 9 and 6 kyr ago. Nature, 411(6835): 290–293

Oviatt CG, Madsen DB, Miller DM, Thompson RS, McGeehin JP (2015). Early Holocene Great Salt Lake, USA. Quat Res, 84(1): 57–68

Parsons L A, Loope G R, Overpeck J T, Ault T R, Stouffer R, Cole J E (2017). Temperature and precipitation variance in CMIP5 simulations and paleoclimate records of the Last Millennium. J Clim, 30(22): 8885–8912

Partin J W, Cobb K M, Adkins J F, Clark B, Fernandez D P (2007). Millennial-scale trends in west Pacific warm pool hydrology since the Last Glacial Maximum. Nature, 449(7161): 452–455

Pausata F S R, Zhang Q, Muschitiello F, Lu Z, Chafik L, Niedermeyer E M, Stager J C, Cobb K M, Liu Z (2017). Greening of the Sahara suppressed ENSO activity during the mid-Holocene. Nat Commun, 8(1): 16020

Repinski P, Holmgren K, Lauritzen S E, Lee-Thorp J A (1999). A late Holocene climate record from a stalagmite, Cold Air Cave, Northern Province, South Africa. Palaeogeogr, Palaeoclimatol, Palaeoecol, 150(3): 269–277

Ricketts R D, Johnson T C, Brown E T, Rasmussen K A, Romanovsky V V (2001). The Holocene paleolimnology of Lake Issyk-Kul, Kyrgyzstan: trace element and stable isotope composition of ostracodes. Palaeogeogr, Palaeoclimatol, Palaeoecol, 176(1): 207–227

Schewe J, Levermann A (2017). Non-linear intensification of Sahel rainfall as a possible dynamic response to future warming. Earth Syst Dyn, 8(3): 495–505

Scott L (1999). Vegetation history and climate in the Savanna biome South Africa since 190,000 ka: a comparison of pollen data from the Tswaing Crater (the Pretoria Saltpan) and Wonderkrater. Quat Int, 57–58: 215–223

Shakun JD, Burns SJ, Fleitmann D, Kramers J, Matter A, Al-Subary A (2007). A high-resolution, absolute-dated deglacial speleothem record of Indian Ocean climate from Socotra Island, Yemen. Earth Planet Sci Lett, 259(3): 442–456

Shaw P A, Bateman M D, Thomas D S G, Davies F (2003). Holocene fluctuations of Lake Ngami, Middle Kalahari: chronology and responses to climatic change. Quat Int, 111(1):23–35

Shi J, Yan Q (2019). Evolution of the Asian-African monsoonal precipitation over the last 21 kyr and the associated dynamic mechanisms. J Clim, 32(19): 6551–6569

Smagorinsky J (1963). General circulation experiments with the primitive equations. Mon Weather Rev, 91(3): 99–164

Springer G, Rowe H, Hardt B, Edwards R, Cheng H (2008). Solar forcing of Holocene droughts in a stalagmite record from West Virginia in east-central North America. Geophys Res Lett, 35

Stansell N D, Rodbell D T, Licciardi J M, Sedlak C M, Schweinsberg A D, Huss E G, Delgado G M, Zimmerman S H, Finkel RC (2015). Late Glacial and Holocene glacier fluctuations at Nevado Huaguruncho in the Eastern Cordillera of the Peruvian Andes. Geology, 43(8): 747–750

Stein R, Fahl K, Gierz P, Niessen F, Lohmann G (2017a). Arctic Ocean sea ice cover during the penultimate glacial and the Last Interglacial. Nat Commun, 8(1): 373

Stein R, Fahl K, Schade I, Manerung A, Wassmuth S, Niessen F, Nam S I (2017b). Holocene variability in sea ice cover, primary production, and Pacific-water inflow and climate change in the Chukchi and East Siberian Seas (Arctic Ocean). J Quaternary Sci, 32(3): 362–379

Stocker T F, Johnsen S J (2003). A minimum thermodynamic model for the bipolar seesaw. Paleoceanography, 18(4): 1087

Tierney J E, Ummenhofer C C, deMenocal P B (2015). Past and future rainfall in the Horn of Africa. Sci Adv, 1(9): e1500682

Tierney JE, Russell JM, Huang Y, Damsté JSS, Hopmans EC, Cohen AS (2008). Northern Hemisphere Controls on Tropical Southeast African Climate During the Past 60,000 Years. Science, 322(5899): 252–255

Vaks A, Bar-Matthews M, Ayalon A, Schilman B, Gilmour M, Hawkesworth CJ, Frumkin A, Kaufman A, Matthews A (2003). Paleoclimate reconstruction based on the timing of speleothem growth and oxygen and carbon isotope composition in a cave located in the rain shadow in Israel. Quat Res, 59(2): 182–193

van Breukelen MR, Vonhof HB, Hellstrom JC, Wester WCG, Kroon D (2008). Fossil dripwater in stalagmites reveals Holocene temperature and rainfall variation in Amazonia. Earth Planet Sci Lett, 275(1): 54–60

Vörösmarty C J, Green P, Salisbury J, Lammers R B (2000). Global water resources: vulnerability from climate change and population growth. Science, 289(5477): 284–288

Wagner J D M, Cole J E, Beck J W, Patchett P J, Henderson G M, Barnett H R (2010). Moisture variability in the southwestern United States linked to abrupt glacial climate change. Nat Geosci, 3(2): 110–113

Wang X F, Auler A S, Edwards R L, Cheng H, Ito E, Wang Y J, Kong X G, Solheid M (2007). Millennial-scale precipitation changes in southern Brazil over the past 90,000 years. Geophys Res Lett, 34: L23701

Wang Y J, Cheng H, Edwards R L, An Z S, Wu J Y, Shen C C, Dorale J A (2001). A high - resolution absolute-dated Late Pleistocene monsoon record from Hulu Cave, China. Science, 294(5550): 2345–2348

Wang Y, Cheng H, Edwards R L, He Y, Kong X, An Z, Wu J, Kelly M J, Dykoski C A, Li X (2005). The Holocene Asian monsoon: links to solar changes and North Atlantic Climate. Science, 308(5723): 854–857

Wang Y, Cheng H, Edwards R L, Kong X, Shao X, Chen S, Wu J, Jiang X, Wang X, An Z (2008). Millennial- and orbital-scale changes in the East Asian monsoon over the past 224,000 years. Nature, 451(7182): 1090–1093

Werne J P, Hollander D J, Lyons T W, Peterson L C (2000). Climate-induced variations in productivity and planktonic ecosystem structure from the Younger Dryas to Holocene in the Cariaco Basin, Venezuela. Paleoceanography, 15(1): 19–29

Williams P W, Neil H L, Zhao J X (2010). Age frequency distribution and revised stable isotope curves for New Zealand speleothems: palaeoclimatic implications. Int J Speleol, 39(2): 99–112

Xia Q, Zhao J, Collerson KD (2001). Early-Mid Holocene climatic variations in Tasmania, Australia: multi-proxy records in a stalagmite from Lynds Cave. Earth Planet Sci Lett, 194(1): 177–187

Xu D, Lu H, Wu N, Liu Z, Li T, Shen C, Wang L (2013). Asynchronous marine-terrestrial signals of the last deglacial warming in East Asia associated with low- and high-latitude climate changes. Proc Natl Acad Sci USA, 110(24): 9657–9662

Yancheva G, Nowaczyk N R, Mingram J, Dulski P, Schettler G, Negendank J F W, Liu J, Sigman D M, Peterson L C, Haug GH (2007). Influence of the intertropical convergence zone on the East Asian monsoon. Nature, 445(7123): 74–77

Yang H, Johnson K R, Griffiths M L, Yoshimura K (2016). Interannual controls on oxygen isotope variability in Asian monsoon precipitation and implications for paleoclimate reconstructions. J Geophys Res Atmos, 121(14): 8410–8428

Yang W, Seager R, Cane M A, Lyon B. (2014). The East African long rains in observations and models. J Clim, 27(19): 7185–7202

Yang Y, Yuan D X, Cheng H, Zhang M L, Qin J M, Lin Y S, Zhu X Y, Edwards R L (2010). Precise dating of abrupt shifts in the Asian Monsoon during the last deglaciation based on stalagmite data from Yamen Cave, Guizhou Province, China. Sci China Earth Sci, 53(5): 633–641

Yuan D, Cheng H, Edwards R L, Dykoski C A, Kelly M J, Zhang M, Qing J, Lin Y, Wang Y, Wu J, Dorale J A, An Z, Cai Y (2004). Timing, Duration, and Transitions of the Last Interglacial Asian Monsoon. Science, 304(5670): 575–578

Zhu F, Emile-Geay J, McKay N P, Hakim G J, Khider D, Ault T R, Steig E J, Dee S, Kirchner J W (2019). Climate models can correctly simulate the continuum of global-average temperature variability. Proc Natl Acad Sci USA, 116(18): 8728–8733

Zwart J A, Sebestyen S D, Solomon C T, Jones S E (2017). The influence of hydrologic residence time on lake carbon cycling dynamics following extreme precipitation events. Ecosystems, 20(5): 1000–1014